CrystEngComm

PAPER

View Article Online
View Journal | View Issue

Cite this: *CrystEngComm*, 2025, **27**, 1879

A Ni-added polyoxometalate: synthesis, structure and catalytic performance†

Zheng-Ge Zhang,[a] Zhen-Wen Wang,[a] Yu Wang,[a] Juan Chen,[a] Yue-Lin Wang*[b] and Guo-Yu Yang *[a]

Received 16th January 2025,
Accepted 11th February 2025

DOI: 10.1039/d5ce00060b

rsc.li/crystengcomm

A Ni_6-added polyoxometalate, $(NH_4)_{0.5}Cs_{1.5}K_4Na_3[Ni(H_2O)_6][\{BO(OH)_2\}_2Ni_6(OH)(H_2O)_6(SiW_{10}O_{37})_2]\cdot 8H_2O$ (**1**), was made with the guidance of the "lacunary-directing synthesis" strategy using a hydrothermal method and characterized by single crystal/powder X-ray diffraction, solid-state UV-vis spectroscopy, FT-IR spectroscopy, and thermogravimetric analysis. The polyoxoanion of **1** could be conceptually constructed by the synergistic directing effect of two dilacunary B-α-$SiW_{10}O_{37}$ fragments linked by a central $[\{BO(OH)_2\}_2Ni_6(OH)(H_2O)_6]^{9+}$ ($\{B_2Ni_6\}$) *via* Ni–O–W and Ni–O–Si linkages. The $\{B_2Ni_6\}$ cluster was composed of a V-shaped $\{Ni_6\}$ core with an angle of 54.6° and further decorated with two $BO(OH)_2$ groups. Furthermore, **1** could be applied in the Knoevenagel condensation reaction as a Lewis catalyst and exhibited excellent catalytic activity under mild reaction conditions.

Introduction

Polyoxometalates (POMs), a class of unique polyoxoanion clusters assembled through condensation reactions of oxygen–metal polyhedra (*e.g.*, MO_n, n = 4, 5 or 6, M = Mo^{VI}, W^{VI}, V^{V}, Nb^{V}, or Ta^{V}) serving as fundamental structural units, have captivated the attention of researchers for about two hundred years owing to their significant applications spanning various domains such as catalysis, magnetism, and optical materials.[1–5] POMs are known as "electron sponges" boasting of abundant surface oxygen atoms capable of storing and transferring electrons. Saturated POMs remove one or several MO_6 units to transform into lacunary POMs, which can serve as Lewis bases and further incorporate a variety of transition metals (TMs) that function as Lewis acids into their structures to significantly affect their properties.[6] Therefore, POMs can exhibit the dual roles of a Lewis acid and Lewis base depending on the specific environmental conditions.[7] Up to now, a multitude of TM-added POMs (TMAPs) have been reported.[8–11]

The synthetic methods for TMAPs mainly encompass a conventional aqueous solution-based method and hydrothermal method. Under hydrothermal conditions, the reactants tend to exhibit higher solubility because of high pressure and high temperature conditions; besides, the reduced viscosity of water further promotes the diffusion process and is conducive to the formation of high-quality and well-shaped crystals. Among TMs, nickel stands out as one of the most abundant elements in the Earth's crust, playing a crucial role in various applications.[12] Consequently, plenty of research studies have been conducted on exploring Ni-added POMs (NiAPs) over the past few years.[13,14] Guided by the strategy of "lacunary-directed synthesis" (LDS), we have successfully obtained an array of innovative NiAPs with distinctive physicochemical properties under hydrothermal conditions.[15–20] Among them, a collection of Ni_6-based TMAPs with Ni^{2+} arranged in a planar triangular shape have received extensive coverage, such as $[(btc)Ni_6(\mu_3\text{-}OH)_3(H_2O)_5(B\text{-}\alpha\text{-}PW_9O_{34})]^{3-}$ (btc = 1,2,4-benzenetricarboxylate)[16] and $[Ni_6(\mu_3\text{-}OH)_3(H_2O)_6(enMe)_3(B\text{-}\alpha\text{-}SiW_9O_{34})]^{-}$ (enMe = 1,2-diaminopropane).[20] However, Ni_6-sandwiched by different POM fragments were reported less.[21–24] Therefore, the construction of sandwiched NiAPs with more Ni^{2+} remains a highly appealing area.

NiAPs can be functionalized through the incorporation of organic/inorganic ligands. The design and synthesis of inorganic–organic hybrid materials by introducing organic ligands to substitute terminal water molecules bound to Ni^{2+} ions have received considerable attention.[25–27] However, studies on NiAPs modified with inorganic ligands are relatively few. Borates, a significant category of inorganic materials, have

[a] *MOE Key Laboratory of Cluster Science, School of Chemistry and Chemical Engineering, Beijing Institute of Technology, Beijing 100081, China. E-mail: ygy@bit.edu.cn, ygy@fjirsm.ac.cn*

[b] *College of Science, Inner Mongolia Agricultural University, Hohhot 010018, China. E-mail: wyl2619@126.com*

† Electronic supplementary information (ESI) available: FT-IR spectra, PXRD patterns, TG curves, and CIF files of **1**. CCDC 2413857. For ESI and crystallographic data in CIF or other electronic format see DOI: https://doi.org/10.1039/d5ce00060b

garnered substantial interest due to their diverse structures and potential applications in luminescence, mineralogy and nonlinear optical phenomena.[28–31] Distinct from simple inorganic groups such as AsO_4, CO_3 and PO_4, which support or decorate TM clusters in a single manner,[32] a boron atom can coordinate with three or four oxygen atoms to form a BO_3 planar triangle or BO_4 tetrahedron, respectively.[33,34] Furthermore, a series of small cluster units can be constructed by linking BO_3 and BO_4 by shared vertices and edges. Their bridging oxygen and hydroxyl groups are capable of substituting terminal water molecules or condensing with hydroxyl groups of TM clusters. Up to now, the successful combination of inorganic boron species with sandwiched NiAPs is limited; two cases have been reported, including $[Ni_6(OH)(BO_3)_2(dien)_2(B\text{-}\alpha\text{-}SiW_{10}O_{37})_2]^{15-}$,[24] and $[(\{Ni_8(\mu_6\text{-}O)(OH)_2\}@\{B_3O_6(OH)_3\}_2)@(B\text{-}\alpha\text{-}GeW_9O_{34})_2]^{20-}$.[35]

Based on the above-mentioned considerations, we endeavored to incorporate inorganic boron into NiAPs, anticipating structural innovation and performance enhancement. In this work, we successfully made a boron-containing NiAP (BNiAP), $(NH_4)_{0.5}Cs_{1.5}K_4Na_3[Ni(H_2O)_6][\{BO(OH)_2\}_2Ni_6(OH)(H_2O)_6(B\text{-}\alpha\text{-}SiW_{10}O_{37})_2]\cdot 8H_2O$ (**1**). **1** features two dilacunary Keggin-type $B\text{-}\alpha\text{-}SiW_{10}O_{37}$ ($\{SiW_{10}\}$) units linked by an interesting metal–nonmetal hybrid cluster $[\{BO(OH)_2\}_2Ni_6(OH)(H_2O)_6]^{9+}$ ($\{B_2Ni_6\}$), which is from the hydroxyl condensation reaction between $B(OH)_3$ and μ_3-OH on the $\{Ni_6\}$ cluster. **1** is the first example of a B-containing Ni_6-sandwiched BNiAP without organic amine substitution. Furthermore, **1** exhibits excellent catalytic activity for the Knoevenagel condensation reaction.

Experimental

Materials and methods

The precursor $K_8Na_2[A\text{-}\alpha\text{-}SiW_9O_{34}]\cdot 25H_2O$ was made following a previously reported procedure.[36] Other chemicals in this experiment were purchased commercially without further purification. The Fourier transform-infrared (IR) spectra were collected on a Thermo Fisher Scientific Nicolet iS10 FT-IR within the range of 400–4000 cm^{-1}. Powder X-ray diffraction (PXRD) data were recorded on a Bruker D8 Advance X-ray diffractometer, equipped with Mo Kα radiation (λ = 1.54056 Å) scanning from 5 to 50°. The optical band gap of **1** was determined and estimated from the UV-vis diffuse reflectance spectra (200–800 nm), utilizing a Shimadzu UV3600 spectrometer (Shimadzu, Kyoto, Japan). The thermal stability of **1** was evaluated through thermogravimetric analysis (TGA), employing a Mettler Toledo TG/DSC 1100 analyzer (Mettler Toledo, Zurich, Switzerland). The testing temperature ranged from 25 to 1000 °C in air with a heating rate of 10 °C min^{-1}. The reactants and products in the Knoevenagel condensation reaction were quantified using a GC-2014C gas chromatograph.

Synthesis of 1

$K_8Na_2[A\text{-}\alpha\text{-}SiW_9O_{34}]\cdot 25H_2O$ (0.341 g, 0.142 mmol), $Ni(Ac)_2\cdot 4H_2O$ (0.242 g, 0.973 mmol), $K_2B_4O_7\cdot 4H_2O$ (0.101 g, 0.331 mmol), $NH_4B_5O_8\cdot 4H_2O$ (0.112 g, 0.412 mmol), NH_4Cl (0.150 g, 2.804 mmol) and CsCl (0.080 g, 0.475 mmol) were added to a mixture solution comprising 2 mL of distilled water and 2 mL of *N*,*N*-dimethylformamide. The resulting mixture was stirred for 2 h and its pH was adjusted to 8.2 using a 4.0 M NaOH solution. The final emulsion was sealed in a 25 mL Teflon-lined bomb and heated at 100 °C for 4 days. After cooling to ambient temperature, green block crystals of **1** can be obtained. Yield: 9.06% (based on $K_8Na_2[A\text{-}\alpha\text{-}SiW_9O_{34}]\cdot 25H_2O$). IR (KBr pellet, cm^{-1}): 3427(vs), 1626(vs), 1398(vs), 1249(s), 1122(w), 984(s), 945(s), 885(vs), 810(s), 749(w), 706(s).

Single crystal structure determination

A single crystal with a regular shape, appropriate size and good quality was selected and adhered to the top of a glass filament using AB adhesive. The diffraction data for **1** were collected on a Gemini A Ultra diffractometer (Mo Kα radiation, λ = 0.71073 Å) under ambient temperature. The structure was solved by the intrinsic phasing method using ShelXT[37] and refined based on the F^2 by full-matrix least-squares method using the ShelXL[38] program package embedded in Olex2 software.[39] The impact of disordered water molecules on the diffraction data for **1** was investigated by the application of the SQUEEZE technique within PLATON.[40] The crystallographic data and structural refinements are listed in Table 1.

Results and discussion

Synthesis

Since 2007, our group has persistently applied hydrothermal synthesis techniques to the addition reactions of lacunary POM clusters. We observed that the incorporation of organic amines with potent coordination abilities can effectively increase the structural dimensionality.[25] Nonetheless, this

Table 1 The crystallographic data and structure refinement for **1**

Compound	**1**
Empirical formula	$B_2Cs_{1.5}H_{47}K_4Na_3Ni_7O_{101}Si_2W_{20}$
Formula weight	6260.48
Crystal system	Orthorhombic
Space group	*Pnma*
a, Å	37.466(3)
b, Å	14.8831(9)
c, Å	18.3908(16)
V, $Å^3$	10254.9(13)
Z	4
D_c, g cm^{-3}	4.028
μ, mm^{-1}	24.415
F(000)	10892.0
T, K	298
Radiation	Mo Kα (λ = 0.71073 Å)
GOF on F^2	1.094
Final *R* indices $[I > 2\sigma(I)]^a$	R_1 = 0.0728, wR_2 = 0.1292
R indices (all data)	R_1 = 0.1215, wR_2 = 0.1423

[a] $R_1 = \sum||F_o| - |F_c||/\sum|F_o|$. $wR_2 = [\sum w(F^2{}_o - F^2{}_c)^2/\sum w(F^2{}_o)^2]^{1/2}$.

also results in a decrease in some of the available nickel coordination sites and impedes the binding of additional ligands. Consequently, the use of similar organic amines is controlled to balance the coordination environment.

In this work, the formation of crystal phases was influenced by the ratio of the reactants, reaction temperature, pH and time. Parallel experiments were performed under both temperatures above and below 100 °C during the reactions, but only limited precipitates were observed. In addition, the optimal molar ratio of the precursor to $Ni(Ac)_2{\cdot}4H_2O$ should be maintained between 1 : 6.5 and 1 : 8, and the pH should be limited in the range of 8.0 to 8.5.

Crystal structure

1 is a sandwiched banana-type POM and crystallizes in the orthorhombic space group *Pnma* (Table 1), which comprises one polyoxoanion of $[\{BO(OH)_2\}_2Ni_6(\mu_4\text{-}OH)(H_2O)_6(B\text{-}\alpha\text{-}SiW_{10}O_{37})_2]^{11-}$ (**1a**, Fig. 1a and b), one free $[Ni(H_2O)_6]^{2+}$, and 1.5 Cs^+, 4 K^+, 3 Na^+, 0.5 NH_4^+, and 8 crystalline water molecules (Fig. S1†). Two B-α-$SiW_{10}O_{37}$ ($\{SiW_{10}\}$) are linked by the central $[\{BO(OH)_2\}_2Ni_6(\mu_4\text{-}OH)(H_2O)_6]^{9+}$ ($\{B_2Ni_6\}$) *via* the Ni–O–W and Ni–O–Si bonds, resulting in an intriguing banana-shaped **1a** (Fig. 1c). The $\{B_2Ni_6\}$ is made of a $[Ni_6(OH)(H_2O)_6]^{11+}$ ($\{Ni_6\}$) core decorated with two $[BO(OH)_2]^-$ ($\{B\}$) (Fig. 1d). The $\{B\}$ units originate from the depolymerization of the reactants $K_2B_4O_7{\cdot}4H_2O/NH_4B_5O_8{\cdot}4H_2O$. Two $\{B\}$ units connect the $\{Ni_6\}$ by two bridging oxygen (O22), leading to the formation of the distinctive B-decorated $\{B_2Ni_6\}$ cluster. O22 is deprotonated and terminal oxygens (O47/48) are monoprotonated, as confirmed by bond valence sum (BVS) calculations (Table S1†). The B–O bond lengths in the $[BO(OH)_2]^-$ groups are in the range of 1.356–1.441 Å. All W atoms exhibit a six coordinated octahedral geometry, with the W–O bond lengths ranging from 1.703 to 2.362 Å.

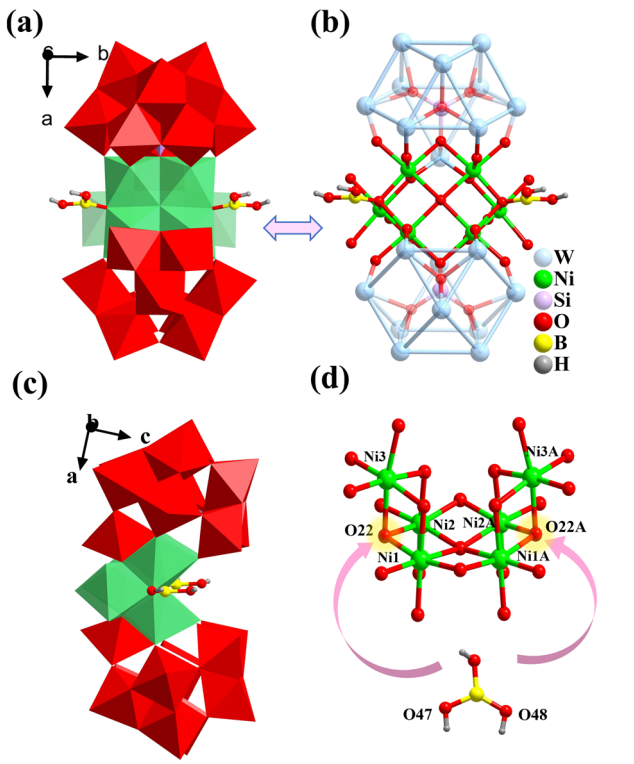

Fig. 1 (a) The view of **1a**; (b) the simplified diagram of **1a**; (c) banana-shaped **1a**; (d) ball and stick diagram of the $\{Ni_6\}$ core and $B(OH)_3$ group. Symmetry code: #: *x*, 1/2 − *y*, *z*. Color labels for polyhedra: WO_6, red; SiO_4, purple; NiO_6, green.

Interestingly, **1a** contains 2 $\{SiW_{10}\}$ subunits derived from $\{A\text{-}\alpha\text{-}SiW_9\}$. Commonly, some TMAPs incorporate $\{SiW_{10}\}$ that often arise from the corresponding dilacunary precursors. For example, $K_{24}[\{\beta\text{-}Ti_2SiW_{10}O_{39}\}_4]{\cdot}50H_2O$,[41] its $\{SiW_{10}\}$ was introduced by the isomerisation of the dilacunary precursor $K_8[\gamma\text{-}SiW_{10}O_{36}]$. The reports on $\{SiW_{10}\}$ from the isomerisation of trilacunary XW_9O_{34} (X = Si/Ge/P) precursors are less common. Several interesting examples, $[Ti_6O_6(A\text{-}\alpha\text{-}1,2\text{-}PW_{10}O_{37})_3]^{15-}$,[42] $[Ti_6O_6(A\text{-}\alpha\text{-}SiW_{10}O_{37})_3]^{18-}$, and $[Ti_{10}O_{11}(A\text{-}\alpha\text{-}SiW_{10}O_{37})_2(SiW_9O_{35})_2]^{26-}$,[43] where $\{A\text{-}\alpha\text{-}SiW_{10}\}$ or $\{A\text{-}\alpha\text{-}PW_{10}\}$ was derived from the transformation of $\{A\text{-}\alpha\text{-}SiW_9\}$ or $\{A\text{-}\alpha\text{-}PW_9\}$ under hydrothermal conditions, without isomerization between A and B types were observed. Because of the stability of trilacunary Keggin-POM units, the formation of $\{B\text{-}\alpha\text{-}SiW_{10}\}$ derived from the precursor $\{A\text{-}\alpha\text{-}SiW_9\}$ rarely occurs in the NiAPs. We supposed that one plausible pathway for the formation of $\{B\text{-}\alpha\text{-}SiW_{10}\}$ (Fig. 2d): $\{A\text{-}\alpha\text{-}SiW_9\}$ (Fig. 2a) undergoes an isomerization reaction, resulting in the formation of $\{B\text{-}\alpha\text{-}SiW_9\}$ (Fig. 2b), which possesses more active sites and exhibits higher activity. Subsequently, $\{B\text{-}\alpha\text{-}SiW_9\}$ combines with a WO_6 fragment derived from the depolymerization of the precursor to form the $\{B\text{-}\alpha\text{-}SiW_{10}\}$ unit. As for the assembly of the $\{Ni_6\}$ cluster, it can be envisioned as two Ni_3O_{13} clusters ($\{Ni_3\}$) (Fig. 3a) connected *via* shared edges. The angle between two $\{Ni_3\}$ is 54.6° (Fig. 3b). All Ni atoms in the $\{Ni_6\}$ core adopt a distorted octahedral coordination geometry with the Ni–O bond lengths in the range of 1.993–2.174 Å. After BVS calculation, O30 is identified as a μ_4-OH and plays a crucial role in the condensation of this cluster (Fig. 3c).

From another perspective, **1a** can be described as two Ni^{2+} occupying two vacant sites of the $\{B\text{-}\alpha\text{-}SiW_{10}\}$ unit (Fig. 4a), forming the "saturated" Keggin $\{Ni_2SiW_{10}\}$ unit (Fig. 4b). Two $\{Ni_2SiW_{10}\}$ units are connected by a μ_4-OH and two μ_2-O, which in turn connect with two additional Ni ions by two μ_3-OH (O22) and four μ_3-O (O13/20) linkages (Fig. 4c). Subsequently, two μ_3-OH undergo hydroxyl

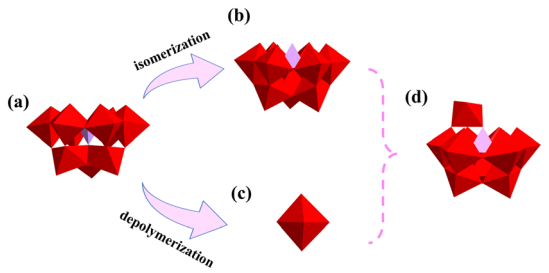

Fig. 2 The polyhedral diagram of (a–d) $\{A\text{-}\alpha\text{-}SiW_9\}$, $\{B\text{-}\alpha\text{-}SiW_9\}$, WO_6 and $\{B\text{-}\alpha\text{-}SiW_{10}\}$ units. Color labels for polyhedra: WO_6, red; SiO_4, purple.

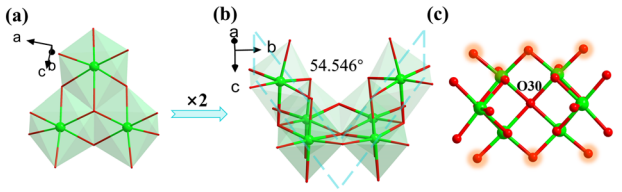

Fig. 3 (a) View of the $\{Ni_3\}$ polyhedron; (b) view of the angle between two $\{Ni_3\}$ clusters; (c) view of the $\{Ni_6\}$ cluster.

condensation reactions with $B(OH)_3$ group moieties and remove two water molecules, forming compound **1** (Fig. 4d and e). From the stacking diagrams, it can be observed that **1a** are distributed and arranged in the –ABA–, –ABA–, and –AAA– manner along the $-a$, $-b$, and $-c$ axes, respectively. The distances between the adjacent polyoxoanions are 37.47 Å, 14.88 Å, and 23.66 Å (Fig. S2†).

Among the known Ni_6-sandwiched POMs, a related structure is $[Ni_6(OH)(BO_3)_2(dien)_2(B\text{-}\alpha\text{-}SiW_{10}O_{37})_2]^{15-}$,[24] in which 2 Ni^{2+} ions bond to six N atoms of 2 dien ligands. Whereas **1** was devoid of steric hindrance originating from the organic ligands, allowing the Ni^{2+} to have more accessible coordination sites, facilitating further substitution of B in later research studies.

FT-IR measurement

The IR spectrum of **1** (Fig. S3†) shows that the peaks observed at 3453 and 1628 cm^{-1} can be attributed to the stretching and bending vibrations of the O–H group. The distinct peak at 1398 cm^{-1} is ascribed to the NH_4^+ group. The peak at 1249 cm^{-1} manifests the existence of B–O bonds. Furthermore, the characteristic peaks of Keggin POM fragments appear in the 680–984 cm^{-1} region. In detail, the typical vibration peaks at 984, 945, 885, and 810 cm^{-1} are attributed to $\nu(Si–O_a)$, $\nu(W–O_t)$, $\nu(W–O_b)$, and $\nu(W–O_c)$ of $\{B\text{-}\alpha\text{-}SiW_{10}\}$ fragments.

Thermogravimetric analysis

The TG curve shows a one-step weight loss of **1** from 25 to 1000 °C (Fig. S4†). The experimental weight loss is 6.42% (calcd: 6.71%), which can be attributed to the loss of 8 lattice water molecules, 12 coordinated water molecules, the dehydration of 5 hydroxyl groups (corresponding to the weight loss of 2.5 water molecules), and 0.5 free NH_4^+ (corresponding to the weight loss of 0.5 NH_3 and 0.25 water molecules).

Powder X-ray diffraction patterns

The experimental powder X-ray diffraction patterns align well with the simulated pattern originating from single-crystal X-ray diffraction (Fig. S5†), indicating that the compound exists in a pure phase. The discrepancies in the intensity may be assigned to the differences in the preferred orientation of the powder sample in the process of collecting the experimental PXRD patterns.

Optical band gap

The solid UV-vis absorption spectrum of **1** (Fig. S5†) is recorded across a wavelength range of 200 to 800 nm. The band gap (E_g) value of the compound is found to be 3.36 eV using the Kubelka–Munk function, indicating its properties of a wide-gap semiconductor.

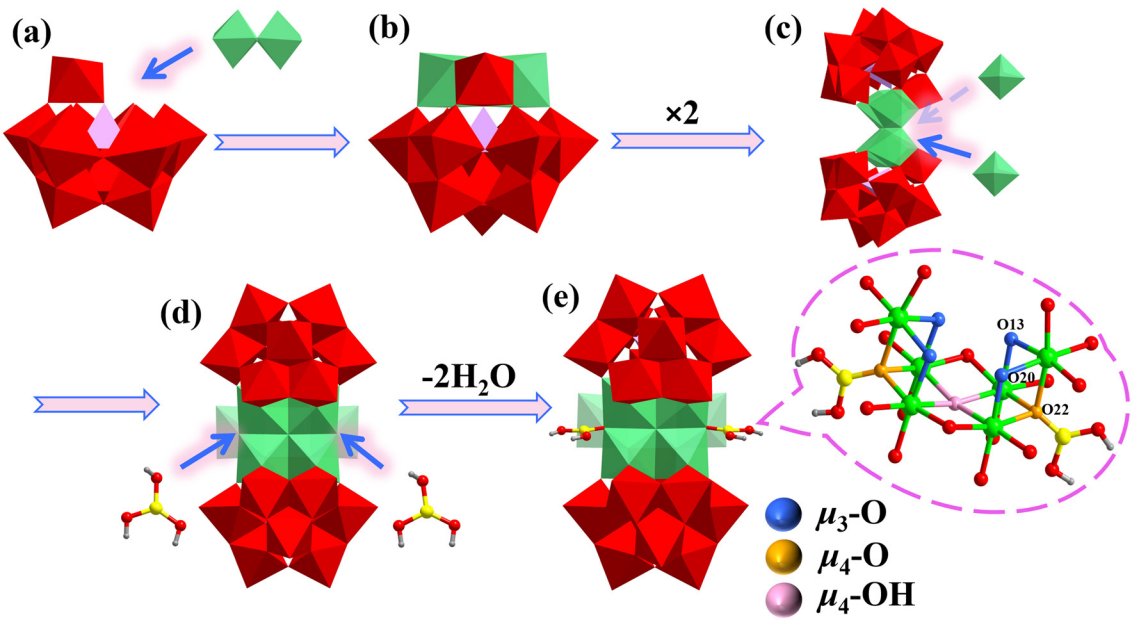

Fig. 4 (a) View of the $\{B\text{-}\alpha\text{-}SiW_{10}O_{37}\}$ unit; (b) view of the "saturated" Keggin-type $\{Ni_2SiW_{10}\}$ unit; (c) polyhedral view of two connected $\{Ni_4(SiW_{10})_2\}$; (d) polyhedral view of $\{Ni_6(SiW_{10})_2\}$; (e) polyhedral view of **1**.

Catalytic activity in Knoevenagel condensation

Knoevenagel condensation of carbonyl compounds with active methylene compounds is renowned as one of the most essential C═C bond formation reactions.[44] It is widely employed in the synthesis of various chemicals and pharmaceutical intermediates, thereby garnering significant attention.[45–47] Traditionally, solid bases and organic amines like triethylamine can act as effective homogeneous catalysts, but their recovery poses significant challenges, especially in liquid-phase reactions and could cause environmental contamination issues.[48] Conversely, some heterogeneous catalysts offer easier recovery but are frequently plagued by issues such as lower efficiency, poor stability and reliance on high-temperature toxic solvents. Consequently, the development of efficient, eco-friendly and recyclable heterogeneous catalysts is of paramount importance. As a heterogeneous catalyst, the POM can function as both a Lewis acid and Lewis base to catalyze reactions, while B with empty orbitals can also be used as a Lewis acid.[49] Thereby, **1** exhibited good catalytic efficiency, which render them highly desirable catalysts for the Knoevenagel condensation reaction.[48,50]

To evaluate the catalytic efficacy of heterogeneous catalyst **1**, an initial model reaction utilizing malononitrile (1.2 mmol) and benzaldehyde (1 mmol) as reactants, **1** as the catalyst, dodecane (0.1 mmol) as the internal standard substance was performed at ambient temperature. This experiment identified the reaction products *via* GC-FID analysis and calculated the conversion rate employing an internal standard method (Fig. S7†). Initially, while keeping other conditions constant, we utilized 0.5 μmol **1** as the catalyst, acetonitrile, ethanediol, ethanol and methanol as the solvents independently and carried out the reaction for 25 minutes to select the best solvent. As depicted in Fig. 5a, the resulting conversion rates were recorded as 10%, 63%, 85% and 94%, respectively. Therefore, methanol was chosen as the preferred solvent for subsequent reactions (Scheme 1). Control experiments were performed to assess the impact of without the catalyst and with 0.5 μmol different catalysts, respectively. After 25 minutes, the conversion rate of benzaldehyde in the absence of the catalyst was 34%, whereas the presence of the catalyst resulted in increased conversion (Fig. 5b), which clearly revealed the superiority of **1** under identical conditions. Besides, the impact of catalyst dosages was explored when **1** is 0.25 μmol, 0.50 μmol, and 1.0 μmol. We can see that 0.5 μmol of **1** is adequate to effectively facilitate the reaction, demonstrating that it has high catalytic activity (Fig. 5c). In subsequent experiments, this amount was maintained. When the reaction time was extended to 50 minutes, the conversion rate of benzaldehyde reaches 100%. In comparison to numerous other POMs, it exhibits a comparatively high catalytic efficiency and facilitates the reaction at an accelerated rate (Table S2†).

Given that **1** shows exceptional catalytic performance in the model reaction, we further broadened the substrate scope

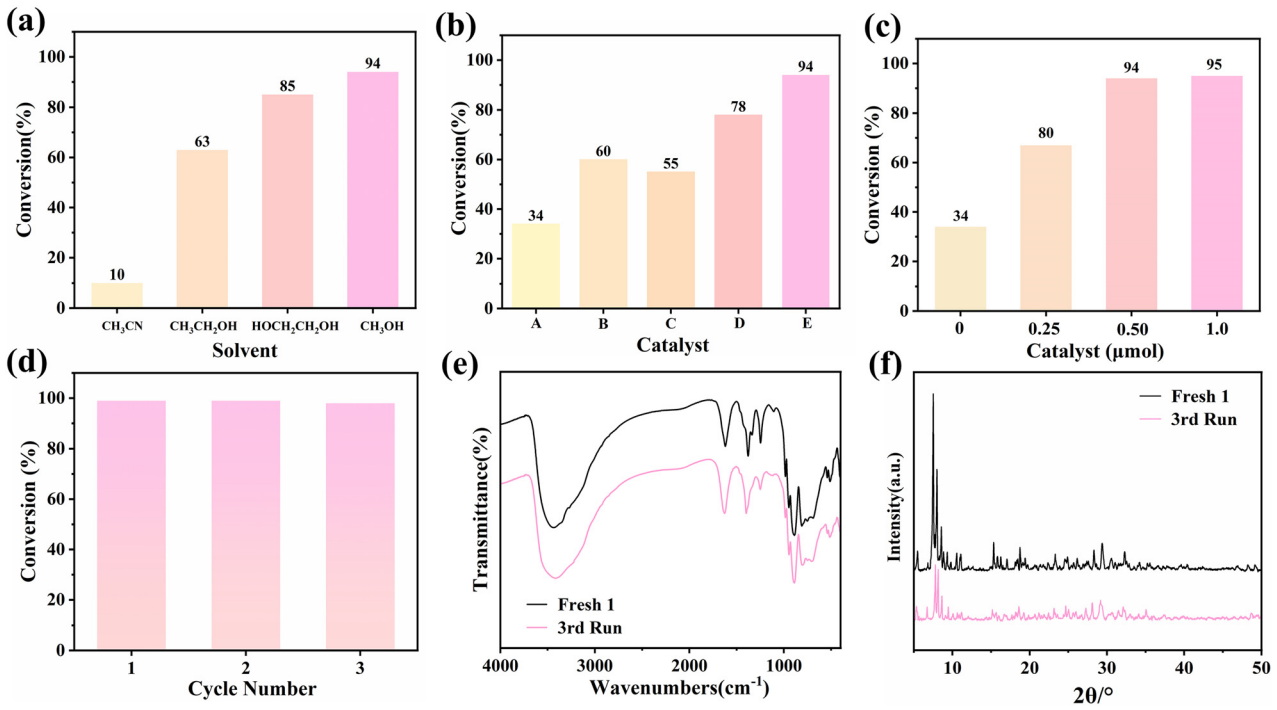

Fig. 5 (a) The comparative experiments of different solvents under the reaction conditions: 1 mmol benzaldehyde, 0.5 μmol of the catalyst, 1.2 mmol malononitrile, and RT, 25 min. (b) The comparative experiments of the different catalysts A: without the catalyst; B: $NH_4B_5O_8{\cdot}4H_2O$; C: $K_2B_4O_7{\cdot}4H_2O$ and D: {A-α-SiW_9}; E: **1**. (c) The conversion rate of benzaldehyde with different amounts of **1**. (d) Recyclability tests of **1** in three cycles. (e) IR spectra of fresh and isolated **1** after the catalytic recycle. (f) The powder X-ray diffraction patterns of fresh and isolated **1** after the catalytic recycle.

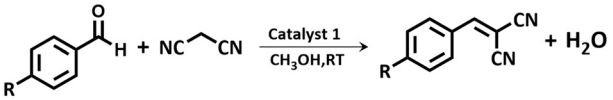

Scheme 1 Knoevenagel condensation reaction.

to comprehensively assess its generality. A series of various substituted benzaldehyde derivatives were systematically investigated under mild conditions. **1** exhibited commendable catalytic efficacy across most substrates (Table 2). Notably, aldehyde derivatives containing electron-accepting groups such as –F (entry 2), –Cl (entry 3), –Br (entry 4–5), –CHO (entry 6), $-NO_2$ (entry 7) and $-CF_3$ (entry 8) underwent complete conversion, achieving conversion rates of 100% after 50 minutes. In contrast, when aldehydes containing electron-donating groups, such as $-CH_3$ (entry 9),

Table 2 Knoevenagel reactions of various aldehydes with malononitrile in the presence of **1**

Entry	Substrate	Product	Temp. (°C)	Time (min)	Yield (%)
1	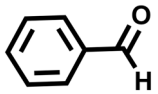	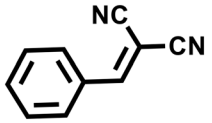	RT	50	100
2	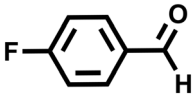	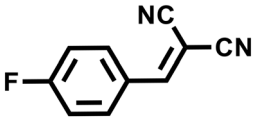	RT	50	100
3	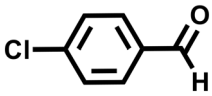	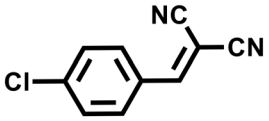	RT	50	100
4	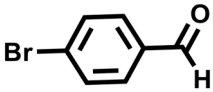	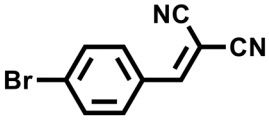	RT	50	100
5	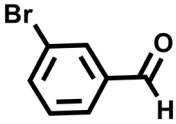	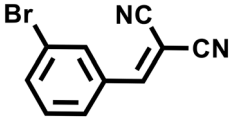	RT	50	100
6	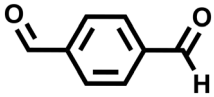	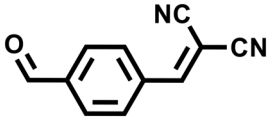	RT	50	100
7	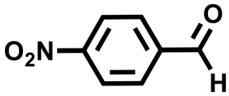	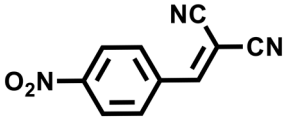	RT	50	100
8	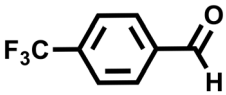	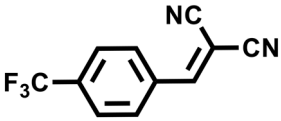	RT	50	100
9	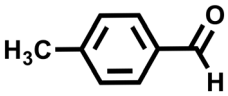	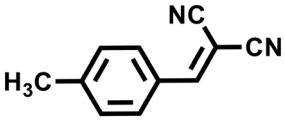	RT	50	90
10	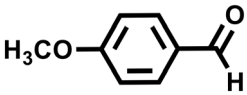	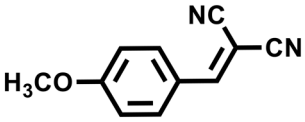	RT	50	91
11		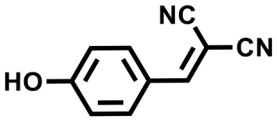	RT	50	88

–OCH_3 (entry 10), and –OH (entry 11), were employed as substrates, we observed a decrease in conversion rates due to the diminished electrophilicity of the carbonyl carbon.

In addition to the reaction conversion rate, the recyclability and stability of heterogeneous catalysts are equally essential evaluation criteria. Consequently, cycling experiments were conducted utilizing benzaldehyde and malononitrile as substrates. **1** was employed in each catalytic period lasting for 50 minutes. Following each reaction, the catalyst underwent centrifugation, methanol washing, and drying and was reused in new reactions. After three cycles, there was no obvious decline of benzaldehyde conversion (Fig. 5d). Furthermore, the IR spectra and PXRD patterns revealed that the peaks corresponding to **1** were well-aligned before and after three cycles, thereby confirming its excellent stability (Fig. 5e and f). In summary, heterogeneous catalyst **1** exhibits remarkable catalytic activity and recyclability.

Conclusions

In conclusion, a NiAP-containing $\{B_2Ni_6\}$ cluster sandwiched between two $\{B\text{-}\alpha\text{-}SiW_{10}\}$ fragments was successfully made through the addition and hydroxyl condensation reactions under hydrothermal conditions. The $\{B_2Ni_6\}$ features an unusual metal–nonmetal oxo-cluster sourced from the hydroxyl condensation reaction between the $B(OH)_3$ moieties and hydroxyl groups of the $\{Ni_6\}$ cluster, which significantly expand the diversity of POM structures. Additionally, catalytic experiments have revealed that **1** is highly effective in facilitating the Knoevenagel condensation reaction, yielding excellent results across a range of substrates. Importantly, incorporating diverse B–O clusters into POMs not only generates innovative composite materials with an exceptional structure but also fosters deeper integration between the fields of inorganic non-metal oxygen clusters and metal oxygen clusters. In future endeavours, we aspire to enhance the exploitation of terminal water coordinated to nickel and explore more applications in other fields.

Data availability

The data used to support the findings of this study are included within the article. Crystallographic data for compound **1** have been deposited at the CCDC under 2413857.

Conflicts of interest

There are no conflicts to declare.

Acknowledgements

This work was supported by the NSFC (No. 21571016, 21831001, and 91122028) and the NSFC for Distinguished Young Scholars (No. 20725101).

Notes and references

1 S. T. Zheng and G. Y. Yang, *Chem. Soc. Rev.*, 2012, **41**, 7623.
2 H. L. Li, C. Lian, D. P. Yin and G. Y. Yang, *Inorg. Chem.*, 2020, **59**, 12842–12849.
3 Z. W. Wang, C. A. Chen and G. Y. Yang, *Dalton Trans.*, 2024, **53**, 9812–9818.
4 Z. Z. Liu, S. L. Huang and G. Y. Yang, *Inorg. Chem.*, 2024, **63**, 12803–12809.
5 Q. Chang, X. Meng, W. Ruan, Y. Feng, R. Li, J. Zhu, Y. Ding, H. Lv, W. Wang, G. Chen and X. Fang, *Angew. Chem.*, 2022, **134**, e202117637.
6 J. W. Zhao, H. P. Jia, J. Zhang, S. T. Zheng and G. Y. Yang, *Chem. – Eur. J.*, 2007, **13**, 10030–10045.
7 S. S. Wang and G. Y. Yang, *Chem. Rev.*, 2015, **115**, 4893–4962.
8 L. Huang, S. S. Wang, J. W. Zhao, L. Cheng and G. Y. Yang, *J. Am. Chem. Soc.*, 2014, **136**, 7637–7642.
9 J. Goura, B. S. Bassil, J. K. Bindra, I. A. Rutkowska, P. J. Kulesza, N. S. Dalal and U. Kortz, *Chem. – Eur. J.*, 2020, **26**, 15821–15824.
10 S. T. Zheng, J. Zhang and G. Y. Yang, *Angew. Chem., Int. Ed.*, 2008, **47**, 3909–3913.
11 Z. W. Wang and G. Y. Yang, *Molecules*, 2023, **28**, 664.
12 X. B. Han, Y. G. Li, Z. M. Zhang, H. Q. Tan, Y. Lu and E. B. Wang, *J. Am. Chem. Soc.*, 2015, **137**, 5486–5493.
13 J. L. Chen, Z. W. Wang, P. Y. Zhang, H. Lv and G. Y. Yang, *Inorg. Chem.*, 2023, **62**, 10291–10297.
14 X. B. Han, Y. G. Li, Z. M. Zhang, H. Q. Tan, Y. Lu and E. B. Wang, *J. Am. Chem. Soc.*, 2015, **137**, 5486–5493.
15 C. Lian, H. L. Li and G. Y. Yang, *Inorg. Chem.*, 2022, **61**, 11335–11341.
16 Z. W. Wang, Q. Zhao, C. A. Chen, J. J. Sun, H. Lv and G. Y. Yang, *Inorg. Chem.*, 2022, **61**, 7477–7483.
17 S. T. Zheng, J. Zhang, J. M. Clemente Juan, D. Q. Yuan and G. Y. Yang, *Angew. Chem., Int. Ed.*, 2009, **48**, 7176–7179.
18 J. W. Zhao, J. Zhang, Y. Song, S. T. Zheng and G. Y. Yang, *Eur. J. Inorg. Chem.*, 2008, **2008**, 3809–3819.
19 S. T. Zheng, J. Zhang, J. M. Clemente Juan, D. Q. Yuan and G. Y. Yang, *Angew. Chem., Int. Ed.*, 2009, **48**, 7176–7179.
20 S. T. Zheng, D. Q. Yuan, H. P. Jia, J. Zhang and G. Y. Yang, *Chem. Commun.*, 2007, 1858–1860.
21 Z. Zhao, B. Zhou, S. Zheng, Z. Su and C. Wang, *Inorg. Chim. Acta*, 2009, **362**, 5038–5042.
22 W. Niu, D. Shi, J. Zhao, X. Cai and L. Chen, *Inorg. Chem. Commun.*, 2012, **17**, 79–83.
23 J. Wang, P. Ma, Y. Shen and J. Niu, *Cryst. Growth Des.*, 2007, **7**, 603–605.
24 Y. Chen, Z. W. Guo, Y. P. Chen, Z. Y. Zhuang, G. Q. Wang, X. X. Li, S. T. Zheng and G. Y. Yang, *Inorg. Chem. Front.*, 2021, **8**, 1303–1311.
25 S. T. Zheng, J. Zhang and G. Y. Yang, *Angew. Chem., Int. Ed.*, 2008, **47**, 3909–3913.
26 S. T. Zheng, J. Zhang, X. X. Li, W. H. Fang and G. Y. Yang, *J. Am. Chem. Soc.*, 2010, **132**, 15102–15103.
27 X. X. Li, Y. X. Wang, R. H. Wang, C. Y. Cui, C. B. Tian and G. Y. Yang, *Angew. Chem., Int. Ed.*, 2016, **55**, 6462–6466.

28 C. A. Chen, W. F. Liu and G. Y. Yang, *Chem. Commun.*, 2022, **58**, 8718–8721.
29 M. Mutailipu, Z. Xie, X. Su, M. Zhang, Y. Wang, Z. Yang, M. R. S. A. Janjua and S. Pan, *J. Am. Chem. Soc.*, 2017, **139**, 18397–18405.
30 J. J. Wang and G. Y. Yang, *Chem. Commun.*, 2017, **53**, 10398–10401.
31 L. Wei, Q. Wei, Z. E. Lin, Q. Meng, H. He, B. F. Yang and G. Y. Yang, *Angew. Chem., Int. Ed.*, 2014, **53**, 7188–7191.
32 C. Lian, H. L. Li and G. Y. Yang, *Inorg. Chem.*, 2021, **60**, 3996–4003.
33 R. Pan, B. F. Yang, G. M. Wang and G. Y. Yang, *Inorg. Chem. Commun.*, 2017, **76**, 15–17.
34 L. Z. Wu, L. Cheng, J. N. Shen and G. Y. Yang, *CrystEngComm*, 2013, **15**, 4483.
35 C. Lian and G. Y. Yang, *Inorg. Chem.*, 2023, **62**, 21409–21415.
36 A. P. Ginsberg, *Inorg. Synth.*, John Wiley & Sons, New York, 1990, vol. 27, pp. 85–100.
37 G. M. Sheldrick, *Acta Crystallogr., Sect. A: Found. Adv.*, 2015, **71**, 3–8.
38 G. M. Sheldrick, *Acta Crystallogr., Sect. A: Found. Crystallogr.*, 2008, **64**, 112–122.
39 O. V. Dolomanov, L. J. Bourhis, R. J. Gildea, J. a. K. Howard and H. Puschmann, *J. Appl. Crystallogr.*, 2009, **42**, 339–341.
40 A. L. Spek, *Acta Crystallogr., Sect. C: Struct. Chem.*, 2015, **71**, 9–18.
41 F. Hussain, B. S. Bassil, L. H. Bi, M. Reicke and U. Kortz, *Angew. Chem., Int. Ed.*, 2004, **43**, 3485–3488.
42 Y. Wang, H. L. Li and G. Y. Yang, *Polyoxometalates*, 2023, **2**, 9140033.
43 H. L. Li, C. Lian and G. Y. Yang, *Inorg. Chem.*, 2021, **60**(21), 16852–16859.
44 A. Lee, A. Michrowska, S. Sulzer Mosse and B. List, *Angew. Chem., Int. Ed.*, 2011, **50**, 1707–1710.
45 U. P. N. Tran, K. K. A. Le and N. T. S. Phan, *ACS Catal.*, 2011, **1**, 120–127.
46 J. Li, G. Liu, L. Shi, Q. Xing and F. Li, *Green Chem.*, 2017, **19**, 5782–5788.
47 Q. Xu, B. Xu, H. Kong, P. He, J. Wang, T. Kannan, P. Ma, J. Wang and J. Niu, *Inorg. Chem.*, 2020, **59**, 10665–10672.
48 Y. K. Zuo, Y. R. Li, Y. Q. Sun, X. X. Li, C. Sun and S. T. Zheng, *Inorg. Chem. Front.*, 2024, **11**, 1993–1997.
49 V. Nori, F. Pesciaioli, A. Sinibaldi, G. Giorgianni and A. Carlone, *Catalysts*, 2021, **12**, 5.
50 M. Y. Dou, D. D. Zhong, X. Q. Huang and G. Y. Yang, *CrystEngComm*, 2020, **22**, 4147–4153.

